Simulation of Fracture Formation in Solid Oxide Fuel Cell Anode Using Peridynamic Modeling Method

Yu Xiang[1] · Zhichao Dong[1] · Zheng Zhong[1] · Zhenjun Jiao[1]

Abstract

Porous cermet materials are widely applied in high-temperature fuel cell electrodes. Fracture formation in the brittle ceramic phase and at the metal–ceramic interface results in mechanical damages and irreversible performance degradation to the electrode performance. In this work, an ordinary state-based peridynamic (OSB-PD) approach is proposed to simulate the formation of fractures in solid oxide fuel cell (SOFC) anodes based on real microstructures reconstructed using focused ion beam scanning electron microscopy (FIB-SEM) dual-beam technique. The effects of external mechanical loads on anode microstructure strength are investigated quantitatively. The key factors determining anode microstructure strength are analyzed based on the simulation results upon the comparison among different anode microstructures. The simulation method provides an easy-to-use approach for evaluating porous cermet microstructure strength during high-temperature operation, which can also be extended to other composite materials.

Keywords Peridynamic · SOFC · FIB-SEM · Fracture

1 Introduction

Solid oxide fuel cell (SOFC), as an advanced green chemical–electrical energy conversion technique, attracts intense investigations in the last decade. Compared to conventional power generation techniques, SOFCs can achieve high energy conversion efficiency with relatively low emissions [1–5]. With relatively high oxygen ionic conductivity and mechanical strength, yttria-stabilized zirconia (YSZ) is widely used as the electrolyte material of SOFCs. Nickel–yttria-stabilized zirconia (Ni-YSZ) composite cermet is widely used

✉ Zhenjun Jiao
jiaozhenjun@hit.edu.cn

Yu Xiang
xiangyu@stu.hit.edu

Zhichao Dong
surpassdzc@163.com

Zheng Zhong
zhongzheng@hit.edu.cn

[1] School of Science, Harbin Institute of Technology (Shenzhen), Shenzhen 518055, China

in SOFC anode by reducing NiO-YSZ composite co-sintered with dense electrolyte [3, 5]. In real industrial applications, SOFCs, separators, and sealants are compacted to assemble multilayered stacks for a higher power density [5]. As a brittle ceramic material, YSZ usually suffers from a brittle fracture due to stresses introduced by external loading during the fabrication and operation processes of the SOFC stacks [4, 6, 7]. Mechanical damages in YSZ phase, such as fractures caused by stresses, can result in gradual degradation or even severe deterioration in SOFC performance during operation. Investigations have been done to study the harmful effects of macroscale fracture on SOFC performances. Malzbender et al. [8] reported a small specimen testing method to assess the role of residual stresses on brittle fractures of anode-supported SOFCs to address the detrimental effects of fractures on SOFC performance. Laurencin et al. [6] investigated the stress field generated in anode-supported SOFCs in macroscale during high-temperature operation. They reported that the mechanical failure probability of electrodes could be predicted by the Weibull theory based on stress distributions. Sato et al. [9] conducted acoustic emission measurements on monitoring fracture generation processes during SOFC operation. They reported that the acoustic emission signal agreed with the macroscopic fracture generations observed. Xie et al. [10] investigated the initialization of fracture in SOFCs and claimed that fracture could be easily initialized from an edge of a single cell because of the high stress generated during a cooling process. So far, most of the investigations on fracture generation in SOFCs were conducted on a macroscale without considering the real microstructure of SOFC electrodes.

Recently, focused ion beam scanning electron microscopy (FIB-SEM) dual-beam technique was widely used to reconstruct the real three-dimensional (3D) microstructures of SOFC electrodes. [11–14]. Wilson et al. [13] quantified the lengths of triple-phase boundaries (TPBs) and the specific surface areas of different phases based on the real anode microstructure reconstructed by FIB-SEM. The high-precision microstructure information captured could also be used to supply accurate 3D reconstruction for further numerical simulations. Celik et al. [11] investigated the 2D stress distribution evolutions in SOFC anode with a temperature rising from room temperature to 800 C. Xiang et al. [12, 14] reported the 3D thermo-mechanical stresses of several real SOFC anode microstructures during temperature rising. The calculations of mechanical failure probabilities in different anode samples were conducted based on the thermal stress distributions obtained in simulations.

Compared to the effectiveness of conventional numerical simulations of stress distributions in a continuum, the finite element method (FEM) shows no advantages in simulating fracture initiation and propagation. In classical continuum mechanics, the application of conventional FEM always suffers the singularity problem in terms of partial differential equations (PDEs) along the discontinuities such as fracture tips and surfaces [15–20]. It is also quite difficult to get rid of the influences of mesh size and the morphology of precast fracture. To simulate the natural generation of discontinuous or fracture generated during the deformation of a material, a new mathematical framework for continuum mechanics called Peridynamic (PD) theory was proposed by Silling [15]. In the Peridynamic theory, problems were formulated in terms of integral equations rather than the PDEs used in the classical continuum mechanical theory [16]. Various characteristics of dynamic brittle fracture propagations observed in experiments, such as crack branching and secondary cracking, were successfully simulated based on Peridynamic theory [21]. To further verify the accuracy of peridynamics simulation, the results of Peridynamic theory extended finite elements method and cohesive zone model were

compared. It was reported that the crack speeds captured from all methods were in the same order, but the fracture paths in Peridynamic simulations were more in agreement with experimental observations [22]. According to the bond force types, PD theory can be classified into three categories: bond-based (BB), ordinary state-based (OSB), and non-ordinary state-based (NOSB) PD. In the BB-PD, the joint pairwise force vectors between any two different material points are opposite in direction with an identical magnitude. In the OSB-PD, the pairwise force vectors between two material points are in the same direction as a bond, while the force magnitudes could be different. In the NOSB-PD, the direction of force density vector need not be along the deformed bond direction and its magnitude may depend on the collective deformation of all the bond in the horizon [19]. According to the brittle material properties of YSZ, OSB-PD theory was selected to overcome the major limitation in Poisson's ratio for BB-PD theory.

Wang et al. [23] firstly reported the application of PD in 2D to simulate fracture generations in SOFC anode upon temperature rising, and the PD simulation results agreed well with the conventional finite element method. However, the Peridynamics model used in their 2D simulations was limited by several constraints, such as a constant Poisson's ratio of 0.25. In this work, real anode microstructures of three anode samples under different sintering conditions are reconstructed by dual-beam FIB-SEM. Based on these reconstructions, simulations of the von Mises equivalent stress and fracture distributions are conducted using in-house code. Ordinary state-based peridynamics are used in the simulation of 3D reconstruction model to overcome the limitations in previous research. Based on the simulation results, it can be clearly seen that under the external loads, the most dangerous positions in the anode are the initiation and propagation of fracture, which is helpful for anode durability during long-term operation.

2 Peridynamic Modeling

The nonlocal peridynamic (PD) theory of continuous media was initially introduced by Silling [15]. PD theory can be considered as a continuum version of molecular dynamics, with the equation of motion of any material point in continuous media at position $\mathbf{x}$ at time t expressed as

$$\rho(\mathbf{x})\ddot{\mathbf{u}}(\mathbf{x}, t) = \int_{H_x} \left(\underline{\mathbf{T}}(\mathbf{u}' - \mathbf{u}, \mathbf{x}' - \mathbf{x}, t) - \underline{\mathbf{T}}(\mathbf{u} - \mathbf{u}', \mathbf{x} - \mathbf{x}', t) \right) dv_{H_x} + \mathbf{b}(\mathbf{x}, t) \qquad (1)$$

where ρ is the material density, H_x refers to the non-local force horizon, and $\mathbf{b}$ is the body force density. The force state $\underline{\mathbf{T}}$ is expressed in the form of components the force density vectors $\mathbf{t}(k)(j)$.

$$\underline{\mathbf{T}}(x_{(k)}, t) = \begin{Bmatrix} \mathbf{t}(k)(1) \\ \cdot \\ \cdot \\ \cdot \\ \mathbf{t}(k)(\infty) \end{Bmatrix} \qquad (2)$$

The OSB-PD bond force density vector $\mathbf{t}(k)(j)$ is defined as

$$\mathbf{t}(k)(j) = 2\delta \left\{ d \frac{\mathbf{\Lambda}_{(k)(j)}}{\left| \mathbf{\xi}_{(k)(j)} \right|} \left(a_{(k)} \theta_{(k)} - \frac{1}{2} a_{2(k)} T_{(k)} \right) + b_{(k)(j)} \mu \left(s_{(k)(j)} - \alpha T_{(k)} \right) \right\} \frac{\mathbf{\xi}_{(k)(j)} + \mathbf{\eta}_{(k)(j)}}{\left| \mathbf{\xi}_{(k)(j)} + \mathbf{\eta}_{(k)(j)} \right|}$$

$$(3)$$

where a, a_2, b, d are the parameters matrix determined by position matrix and material parameter such as Young's modulus E, Poisson's ratio μ and shear modulus G based on equating the strain energy density in classical continuum mechanics with the one in PD theory [24], which are defined in 3D as

$$a = \frac{1}{2} \left(\kappa - \frac{5}{3} G \right) \quad a_2 = 6\alpha a \quad a_3 = 9\alpha^2 a \quad d = \frac{9}{4\pi\delta^4} \quad b = \frac{15G}{2\pi\delta^5}. \tag{4}$$

In addition, T is the temperature difference from the reference temperature and α is the thermal expansion coefficient of a material. $\mathbf{\xi}$ refers to the relative position vector of two material points, and $\mathbf{\eta}$ is the relative displacement vector of the corresponding material points pair after deformation, which are defined as

$$\mathbf{\xi}_{(k)(j)} = \mathbf{x}_{(j)} - \mathbf{x}_{(k)} \tag{5}$$

$$\mathbf{\eta}_{(k)(j)} = \mathbf{u}_{(j)} - \mathbf{u}_{(k)} \tag{6}$$

where $\mathbf{\Lambda}_{(k)(j)}$ is defined as

$$\mathbf{\Lambda}_{(k)(j)} = \frac{\mathbf{\xi}_{(k)(j)} + \mathbf{\eta}_{(k)(j)}}{\left| \mathbf{\xi}_{(k)(j)} + \mathbf{\eta}_{(k)(j)} \right|} \cdot \frac{\mathbf{\xi}_{(k)(j)}}{\left| \mathbf{\xi}_{(k)(j)} \right|} \tag{7}$$

and the dilatation coefficient $\theta_{(k)}$ is defined as

$$\theta_{(k)} = d \sum_{j=1}^{N} \delta \mu \left(s_{(k)(j)} - \alpha T_{(k)} \right) \frac{\mathbf{y}_{(j)} - \mathbf{y}_{(k)}}{\left| \mathbf{y}_{(j)} - \mathbf{y}_{(k)} \right|} \cdot \frac{\mathbf{x}_{(j)} - \mathbf{x}_{(k)}}{\left| \mathbf{x}_{(j)} - \mathbf{x}_{(k)} \right|} V_{(j)} + 3\alpha T_{(k)} \tag{8}$$

where $V_{(j)}$ is the volume of the material point at $\mathbf{x}_{(j)}$, and $s_{(k)(j)}$ is the bond stretch, which is defined as

$$s_{(k)(j)} = \frac{\left| \mathbf{\xi}_{(k)(j)} + \mathbf{\eta}_{(k)(j)} \right| - \left| \mathbf{\xi}_{(k)(j)} \right|}{\left| \mathbf{\xi}_{(k)(j)} \right|}. \tag{9}$$

A history-dependent parameter μ is defined in PD to quantify the extent of the local damage as

$$\mu \left(\mathbf{x}_{(j)} - \mathbf{x}_{(k)}, t \right) = \begin{cases} 1 & \text{if} \quad s_{(k)(j)} < s_c \\ 0 & \text{otherwise} \end{cases} \tag{10}$$

where s_c is a critical stretch over which the bond force between two material points becomes zero, and the corresponding bond can be considered damaged [16, 25]. In 3D, s_c is defined as [24]

$$s_c = \sqrt{\frac{G_c}{\left(3G + \left(\frac{3}{4}\right)^4 \left(\kappa - \frac{5}{3}G\right)\right)\delta}} \tag{11}$$

where κ and G are the bulk and shear moduli of a material. A local damage can be quantified using φ, the ratio between the number of bonds damaged to the total number of initial bonds surrounding a material point as

$$\varphi(\mathbf{x}, t) = 1 - \frac{\int_{H_\mathbf{x}} \mu(\mathbf{x}' - \mathbf{x}, t)dV'}{\int_{H_\mathbf{x}} dV'} \tag{12}$$

where $\varphi > 0.38$ indicates a complete local damage in this work. In order to obtain the stress distribution based on the above simulation results, the first Piola–Kirchhoff stress σ_0 in OSB PD can be calculated as [18]

$$\boldsymbol{\sigma}_0 = \int_{H_x} \underline{\mathbf{T}}(\boldsymbol{\eta}, \xi, t) \otimes \xi dV \tag{13}$$

where $\otimes$ is the symbol of a dyadic product. The corresponding deformation gradient tensor is defined as

$$\mathbf{F} = (\underline{\mathbf{Y}} * \underline{\mathbf{X}})\mathbf{K}^{-1} \tag{14}$$

where $\underline{\mathbf{X}}$, $\underline{\mathbf{Y}}$ are the reference position vector state and the deformation vector state, respectively, and $\underline{\mathbf{Y}} * \underline{\mathbf{X}}$ is the corresponding tensor product [19]. The shape tensor $\mathbf{K}$ is defined as $\mathbf{K} = \underline{\mathbf{X}} * \underline{\mathbf{X}}$.

According to the conventional continuum mechanics theory, the corresponding Cauchy stress tensor τ can be calculated as [18]

$$\boldsymbol{\tau} = J^{-1}\boldsymbol{\sigma}_0\mathbf{F}^T \tag{15}$$

In this work, all of the anode microstructures reconstructed were digitalized into 3D matrices containing three domains corresponding to Ni, YSZ, and pore phases, respectively. Every reconstruction was then discretized into the finite number of volumes $(160 \times 160 \times 160)$ by defining a specific material point at the center of the volume, which belonged to a material. $\delta = 3\Delta$ is defined as the radius of the horizon $H_\mathbf{x}$, Δ is the grid spacing. For the material points in the range $\xi_{(k)(j)} = \left|\mathbf{x}_{(j)} - \mathbf{x}_{(k)}\right| < \delta - \Delta/2$, a volume correction factor is defined as $v_c(j) = (\delta + \Delta/2 - \xi_{(k)(j)})/\Delta$. Otherwise, the volume correction factor is $v_c(j) = 1$ [24]. Mechanical properties of different materials at SOFC operation temperature are summarized in Table 3. In a simulation, two types of interaction between two material points need to be specified. One is the interaction between the material points with identical material properties. The other is the interaction across the Ni-YSZ interface, where the elastic modulus, bulk modulus, and Poisson ratio of Ni phase and the fracture toughness of YSZ phase were selected to facilitate the simulations [26]. For the boundary conditions set under an external load, the displacements of the material points on a boundary surface along the loading axis were fixed. On the opposite boundary surface, a layer of material points, with a thickness of $\Delta L = 0.4301 \mu m$, was replaced by a dense YSZ plate. A uniform volume force density

was imposed on each material point at $X = L + \Delta L$, as shown in Fig. 2, to simulate an external load. For initial conditions, residual stresses in both Ni and YSZ phases at operation temperature were ignored in this work to facilitate the simulations.

Verlet semi-implicit scheme was applied in time integration to obtain the numerical solution. The average displacement of the boundary cross-section in reconstruction was tracked to monitor the convergence of the simulation. An adaptive dynamic relaxation method [24] was utilized to stabilize the simulation when the external load was not large enough to cause complete damage to the microstructure, while the average displacement of the boundary cross section converged to a steady-state value after a time step. The average displacement of the boundary surface may not converge when a large external load was applied, which resulted in the breaking up of the reconstruction. Then, the simulations were terminated when the average stretch of the reconstruction along the loading direction reached 5%.

3 Modeling Validation

Before the simulations of fracture formation in real anode microstructures were conducted, the OSB-PD model was validated by simulating the fracture formation in notch deep beam (NDB) specimens with preset cracks of different inclinations. In the simulations of validation, a brittle material of rock was used and the corresponding material properties are summarized in Table 2. Three typical inclinations of $\alpha = 0^o$, $\alpha = 30^o$ and $\alpha = 45.9^o$ were selected for the precast cracks. The NDB specimens were subjected to different vertical loads at the central point of the top and two supports at the bottom, as shown in Fig. 3a. Figure 3b−d shows the fracture formation patterns corresponding to the three inclinations under loads of $P = 5.366$ kN, 7.616 kN, and 10.563 kN, respectively. According to the simulation results, it is clearly seen that, no matter what the inclination of the precast crack was, the fractures propagated toward the central loading point from the tip of the precast crack. The fracture formation predicted by the OSB-PD simulations agreed well with the experimental results reported in Ref. [27], which proved the correctness of the model.

Table 1 Parameters of fabrication and microstructure characterizations of anodes S1 to S3

Parameters		S1	S2	S3
Sintering T	^oC	1400	1500	> 1600
Reduction T	^oC	800	800	800
Volume fraction	%			
Ni		21.49	31.68	34.44
YSZ		29.09	37.08	38.49
Pore		49.42	31.24	27.07
Tortuosity factor				
	x-axis	13.53	3.55	3.80
YSZ	y-axis	9.82	3.68	5.15
	z-axis	12.69	3.30	5.64
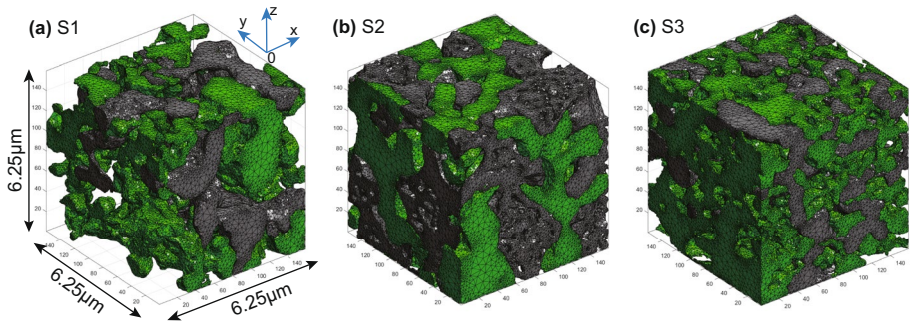
Fig. 1 3D reconstruction images of Ni-YSZ anodes sintered at (**a**) 1400°C, (**b**) 1500°C, and (**c**) > 1600°C using microwave (Gray: Ni; Green: YSZ)

4 3D Microstructure Reconstruction Methods

The SOFC anode used in this work was fabricated using a mixture of commercial YSZ and NiO powders, with a volume ratio of 40% ∶ 60%. The anode was sintered at 1400°C temperature and then reduced at 800°C to obtain Ni-YSZ composite. The composite microstructure was reconstructed using FIB-SEM dual-beam technique. In order to distinguish the pores of the Ni-YSZ composite during the SEM observation, the composite was infiltrated with a low-viscosity epoxy resin under low-pressure atmosphere (ca.15 Pa). After the resin was cured, the sample was polished by using Ar-ion beam cross section polisher for the FIB-SEM observation. A series of 2D cross section images of the sample structure can be obtained by observing the samples prepared by FIB-SEM. Finally, a 3D reconstruction with a size of 6.25 μm×6.25 μm×6.25 μm was accomplished based on the series of segmented 2D image by code written with MATLAB and ImageJ, as shown in Fig. 1a. For comparison, the microstructures of other two anodes were reconstructed. All the stress and fracture distributions in this work were projected onto the tetrahedron meshes generated by CGAL mesh , which is an open-source 3D simplicial mesh generator, to facilitate observations. The three anodes were labeled as

Fig. 2 Illustration of external load boundary conditions in PD modeling (Green: YSZ, gray: Ni, black: pore)
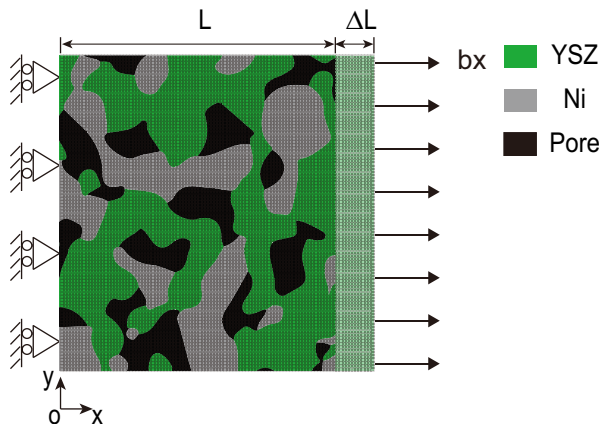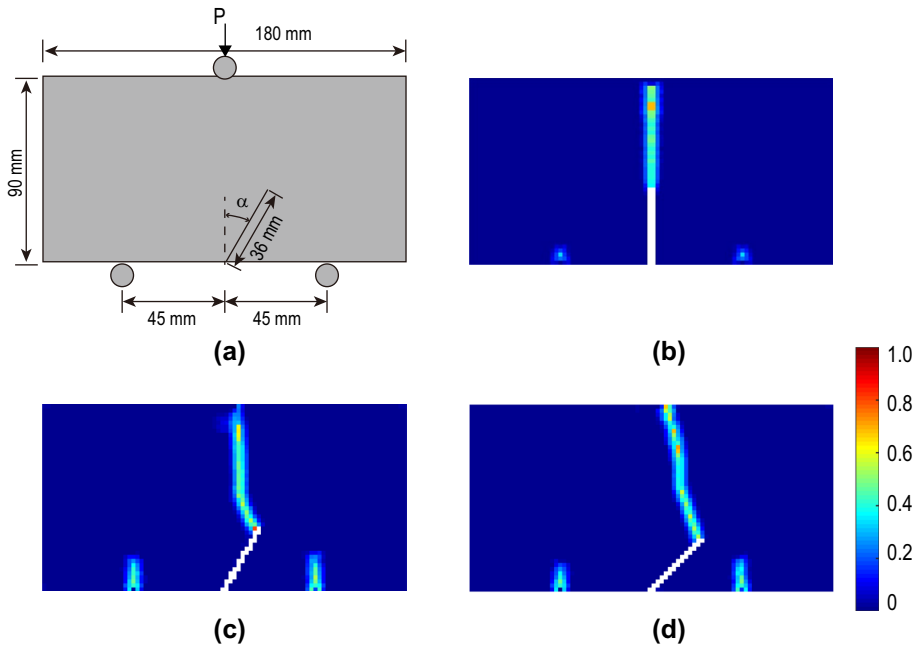
Fig. 3 Illustration of (**a**) the three-point bending strength test on a notch deep beam, and the corresponding simulation results of fracture formation with a pre-crack inclination of (**b**) $\alpha = 0^o$, (**c**) $\alpha = 30^o$, and (**d**) $\alpha = 45.9^o$

S1–S3, with their fabrication conditions and microstructure parameters summarized in Table 1. Details of anode fabrication and image processing procedures are referred to Refs. [28].

5 Results and Discussion

In this section, the simulations of von Mises equivalent stress and fracture distributions in S1 under different external loads are performed firstly. Then, the distributions of fracture in S1 under 20 MPa external load in x, y, and z directions are given. Material properties of Ni and YSZ used in this work are presented in Table 3. Compared with room temperature, Ni becomes very soft in the operating environment. So the elastic modulus of Ni is selected according to Ref. [29].

Table 2 Parameters used in the simulations of the three-point bending strength test on a notch deep beam

Elastic modulus (GPa)	Poisson's ratio	Density kgm^{-3}	Tensile strength (MPa)	Mode I fracture toughness (MPam$^{1/2}$)	Mode II fracture toughness (MPam$^{1/2}$)
3.9	0.25	2410	3.37	0.378	0.234

Table 3 The properties of anode materials used in the PD model [23, 29]

Phases	Elastic modulus	Poisson's ratio	Density	Fracture toughness	Thermal expansion coefficient	Thermal conductivity
	(GPa)		(kgm^{-3})	$(\text{MPam}^{-1/2})$	K^{-1}	$(\text{Wm}^{-1}\text{K}^{-1})$
Ni	4.9	0.310	8800	125	13.5×10^{-6}	60.7
8YSZ	157	0.313	5200	3.5	10.5×10^{-6}	2.1

Figure 4 shows the von Mises stress and the corresponding fracture distributions in the simulations of S1 under both tensile stresses of 5 MPa, 10 MPa, and 20 MPa and compressive stress of −20MPa, respectively. In the images, a dense YSZ plate is hidden, and Ni is displayed as a transparent phase to facilitate the observations of both stress and fracture formation distributions. According to the simulation results, it is seen that external tensile stress of 5 MPa caused no fracture damage to the microstructure, though the maximum von Mises stress reached 1 GPa level in YSZ at several locations highly curved. Under an external tensile load of 10 MPa, limited fractures can be observed formed at Ni-YSZ interfaces, and the area under high von Mises stress was enlarged. When the tensile stress reached 20 MPa, a larger area of regions under high von Mises stress can be observed. In addition, fracture damages can be observed formed at the Ni-YSZ interface in a large area and in YSZ at several locations. This phenomenon, which is hard to be observed in the microstructure reconstructed by FIB-SEM at room temperature, could have significant degradation for the performance of anodes. Compared to the case under 20 MPa tensile stress, an external compressive stress load of 20 MPa only resulted in limited fracture formations at the Ni-YSZ interface and in YSZ, though the high von Mises stress regions are similar to the case of 20 MPa tensile stress. It is clearly seen that the microstructure of S1 shows much higher fracture resistance under a compressive load. Upon the comparison among the four cases, it is seen that the high von Mises stresses concentrate at highly curved regions, which are corresponding to two kinds of fracture formations at the Ni-YSZ interface and in YSZ, respectively. No high von Mises stress was observed in the Ni phase, which was corresponding to its large critical stretch and small elastic modulus. Similar fracture formation phenomena were reported in 2D by Wang et al. [23]. The simulation results in this work are also consistent with the failure probability predictions in our previous work [14], that the Weibull failure probabilities of microstructure S1 under external loads are 0.24%, 15.79%, 100% and 98.9% under tensile loads of 5 MPa, 10 MPa, and 20 MPa and a compressive load of −20 MPa, respectively. The simulation results indicate that the anode strength is dominated by the brittle YSZ skeleton, while Ni behaves as soft material. The mechanical damages are dominated by the formations of fracture under sizeable tensile stress. In the later discussions, we only focus on external loads of tensile stresses.

To verify the isotropy of the fracture formation, the simulation results of S1 under an external load of 20 MPa along *x*-, *y*-, and *z*-axis are compared, as shown in Fig. 5. Dense YSZ plates were displayed transparently to indicate the direction of the external loads. It is seen that fracture formations are distributed differently when the external loading boundary was changed. The result along the *x*-axis shows the largest fracture areas both at the Ni-YSZ interface and in YSZ, while the result along the *y*-axis shows the lightest damages. The degrees of damage in three cases can be attributed to the values
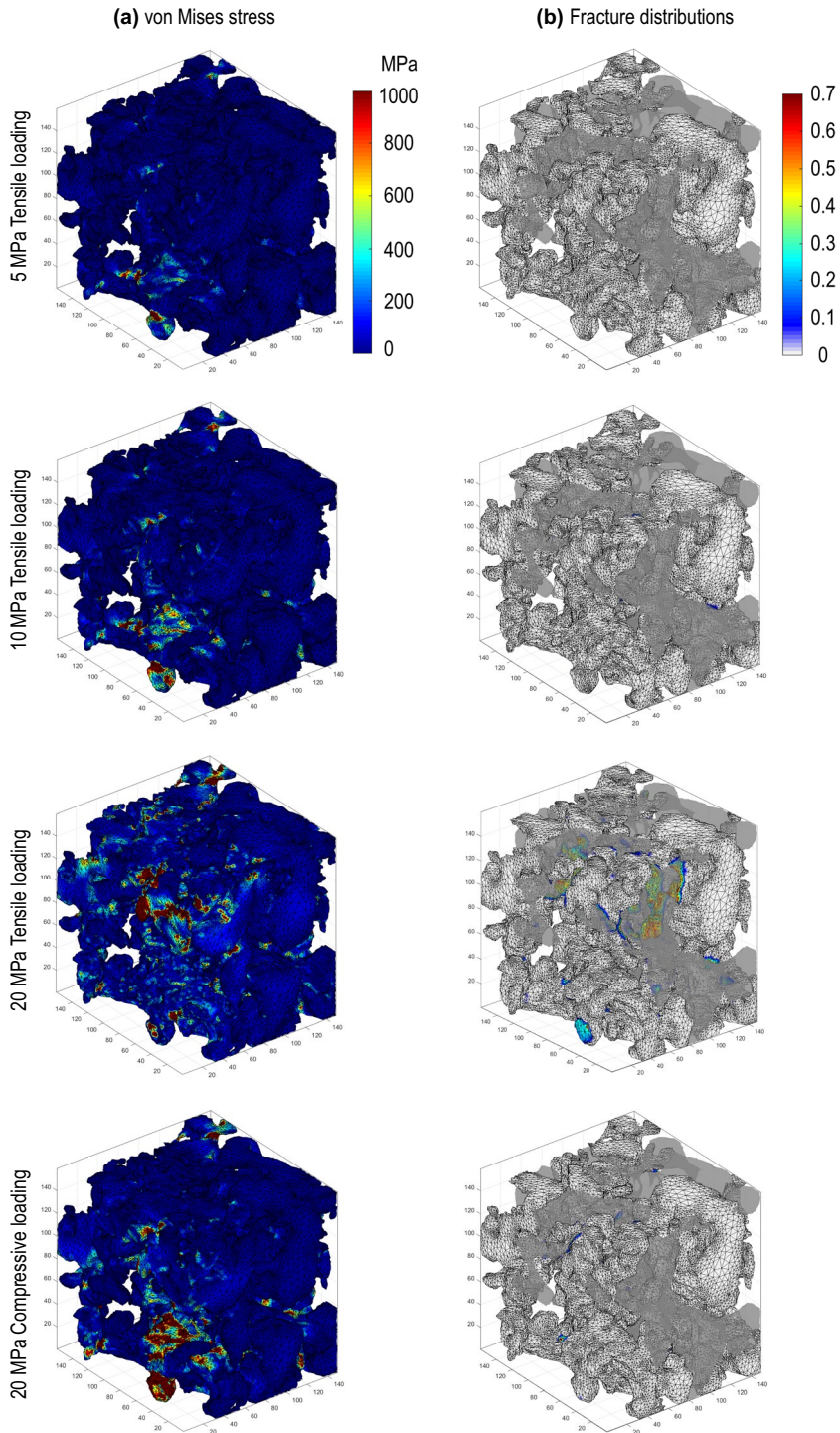
Fig. 4 von Mises stress and fracture distributions in S1 under external tensile loads of 5 MPa, 10 MPa, and 20 MPa and an external compressive load of 20 MPa
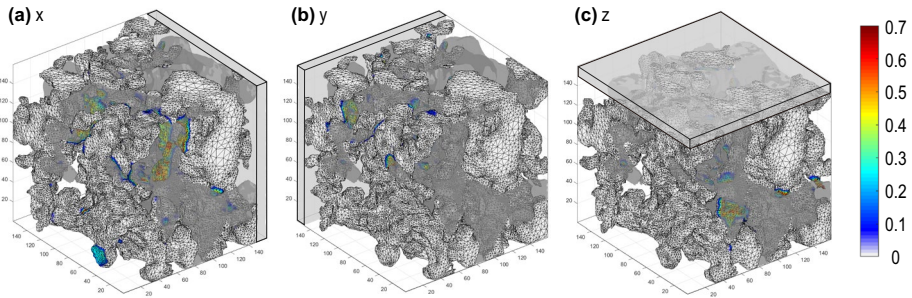
Fig. 5 Fracture distributions in S1 with external tensile loads of 20 MPa along (**a**) *x*- (**b**) *y*-, and (**c**) *z*-axes

of tortuosity factors along three axes, as shown in Table 1. The results indicate that a smaller tortuosity factor enhances the fracture resistance of the anode microstructure under a large tensile load along a specific direction. At the same time, it is also known that the current reconstruction size might not be large enough to represent the microstructure characterization statistically.

To study the influence of microstructure characterization on anode strength, simulations based on S2 and S3 were conducted under two external loads of 5 MPa and 20 MPa along the *x*-axis, with the simulation results shown in Fig. 6. No fracture formations were observed in the simulations for both S2 and S3 under two tensile loads. For a tensile stress load of 5 MPa, no high von Mises stress regions can be observed in both S2 and S3. For a tensile stress load of 20 MPa, only limited areas with small areas were under high von Mises stress at a level of 1 GPa. The much higher anode strength of both S2 and S3 can also be attributed to their low tortuosity factor along all axes, as shown in Table 1. The comparison indicates that the anode strength can be primarily modified using different sintering schemes during an anode fabrication.

In this work, fracture formation simulations based on real SOFC anode microstructures were conducted using PD theory. The simulation results showed the potential of the PD simulation method and revealed the connectivity between anode strength and the key microstructure parameter of the tortuosity factor. It is well known that the anode performance is adversely influenced by a high porosity because of the reduced TPB density [30]. It was proven that a high porosity in anode results in a decrease in YSZ volume fraction so that the tortuosity factor of YSZ, which finally weakens the anode microstructure strength. The simulation results suggest that anode microstructure strength under external loads can be enhanced using a higher sintering temperature or advanced sintering technique with a large temperature ramping rate.
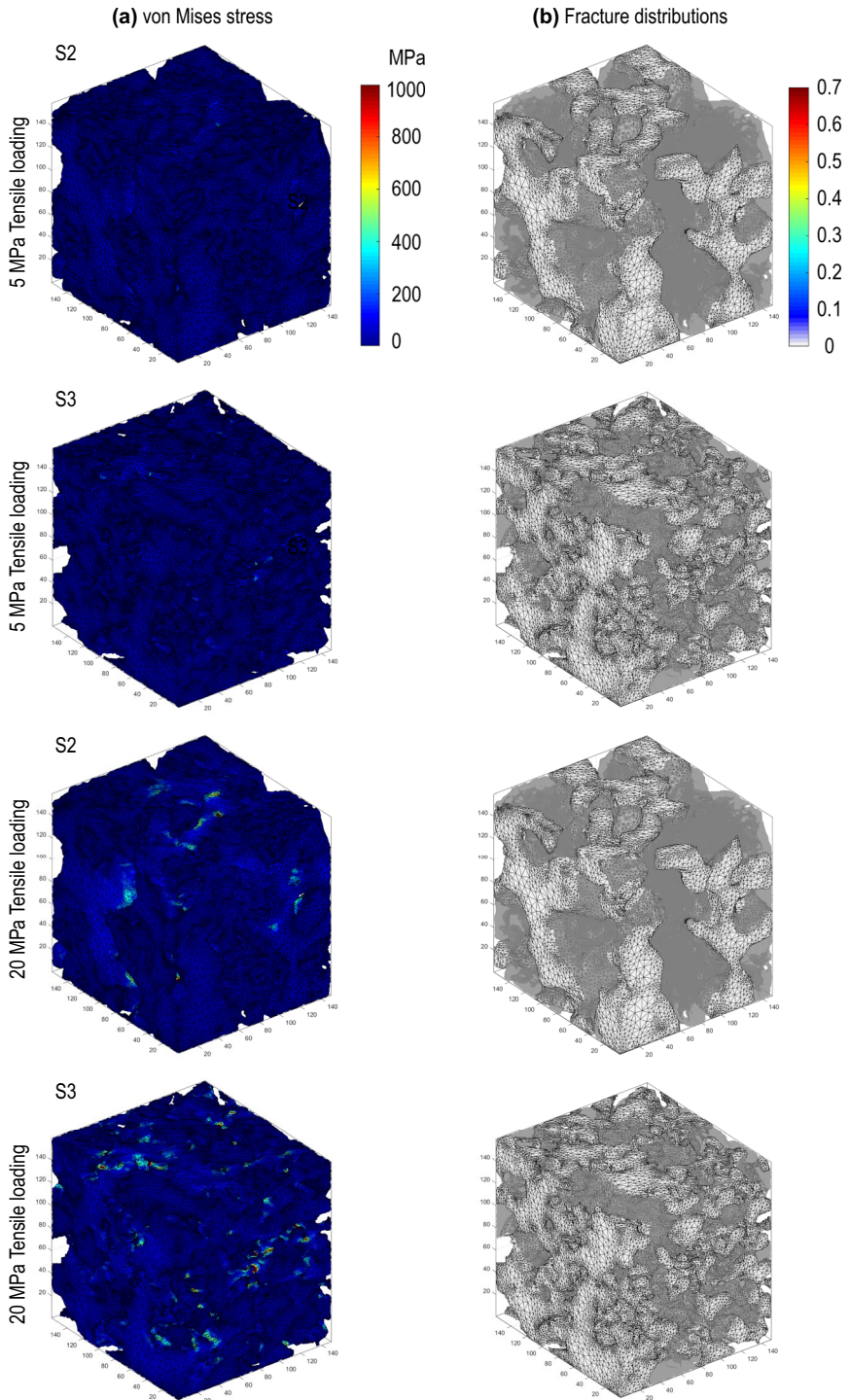
Fig. 6 (**a**) von Mises stress and (**b**) fracture distributions in S2 and S3 under external tensile loads of 5 MPa and 20 MPa, respectively

6 Conclusion

In this paper, OSB-PD method was utilized to simulate the formations of fracture in SOFC anodes under external loads based on the real microstructures reconstructed using FIB-SEM dual-beam technique. The distributions of von Mises stress and local damage at SOFC operation temperature were analyzed systematically. To identify the predominant factor influencing anode strength, the simulations based on the anodes fabricated using different sintering methods were conducted. The comparison among the simulation results indicated that the mechanical strength of an anode under an external load was determined by the tortuosity factor of the YSZ phase, which can be enhanced using different sintering schemes. It was also proven that the fractures formed at the Ni-YSZ interface were the predominant damages to the anode microstructure under a large external load. In future works, the PD simulation method can be improved to predict the mechanical properties of SOFC electrodes in trans-scale by coupling the local environmental parameters in the simulations.

Author Contributions Z. J and Z. Z conceived the project. Z. J prepared the Ni-YSZ anode and reconstructure 3D model. Y. X developed the OSB-PD code and anode fracture simulation. Z. D contributed to the modeling validation section.

Data Availability The data supporting the results are available from the authors upon reasonable request.

Code availability The code written with MATLAB for the multistage reconstruction and the OSB-PD fracture simulation is available from the authors upon reasonable request.

Declarations

Competing interests The authors declare no competing interests.

References

1. Fang XR, Zhu J, Lin ZJ (2018) Effects of electrode composition and thickness on the mechanical performance of a solid oxide fuel cell. Energies 11(7). https://doi.org/10.3390/en11071735
2. Song BW, Ruiz-Trejo E, Bertei A (2017) Brandon NP (2018) Quantification of the degradation of Ni-YSZ anodes upon redox cycling. J Power Sources 374:61–68. https://doi.org/10.1016/j.jpowsour.2017.11.024
3. Wang Y, Walter ME, Sabolsky K, Seabaugh MM (2006) Effects of powder sizes and reduction parameters on the strength of Ni-YSZ anodes. Solid State Ionics 177(17–18):1517–1527. https://doi.org/10.1016/j.ssi.2006.07.010
4. Xu YQ, Wang LL, Zhang QW (2012) Residual stress and thermal stress in Ni/YSZ anode support micro-tubular solid oxide fuel cell. Adv Mater Res 347–353:3228–3231. https://doi.org/10.4028/www.scientific.net/AMR.347-353.3228
5. Yu JH, Park GW, Lee S, Woo SK (2007) Microstructural effects on the electrical and mechanical properties of Ni-YSZ cermet for SOFC anode. J Power Sources 163(2):926–932. https://doi.org/10.1016/j.jpowsour.2006.10.017
6. Laurencin J, Delette G, Dupeux M, Lefebvre-Joud F (2007) A Numerical Approach to Predict the SOFC Fracture: The Case of an Anode Supported Cell. ECS Trans 7(1):677–686. https://doi.org/10.1149/1.2729153

7. Liu WN, Sun X, Khaleel MA, Qu JM (2009) Global failure criteria for positive/electrolyte/negative structure of planar solid oxide fuel cell. J Power Sources 192(2):486–493. https://doi.org/10.1016/j.jpowsour.2009.03.012

8. Malzbender J, Steinbrech RW, Wessel E (2009) Brittle fracture studies of solid oxide fuel cells. Key Eng Mater 409:81–93. https://doi.org/10.4028/www.scientific.net/KEM.409.81

9. Sato K, Hashida T, Yugami H, Yashiro K, Kawada T, Mizusaki J (2006) Characteristics of Damage and Fracture Process of Solid Oxide Fuel Cells Under Simulated Operating Conditions By Using Ae Method. J Acoust Emiss 24:215–221

10. Xie JM, Hao WQ, Wang FH (2019) Crack propagation of planar and corrugated solid oxide fuel cells during cooling process. Int J Energy Res 43(7):3020–3027. https://doi.org/10.1002/er.4369

11. Celik S, Ibrahimoglu B, Mat MD, Kaplan Y, Veziroglu TN (2015) Micro level two dimensional stress and thermal analysis anode/electrolyte interface of a solid oxide fuel cell. Int J Hydrogen Energy 40(24):7895–7902. https://doi.org/10.1016/j.ijhydene.2014.10.057

12. Clague R, Shearing PR, Lee PD, Zhang Z, Brett DJ, Marquis AJ, Brandon NP (2011) Stress analysis of solid oxide fuel cell anode microstructure reconstructed from focused ion beam tomography. J Power Sources 196(21):9018–9021. https://doi.org/10.1016/j.jpowsour.2010.12.097

13. Wilson JR, Kobsiriphat W, Mendoza R, Chen HY, Hiller JM, Miller DJ, Thornton K, Voorhees PW, Adler SB, Barnett SA (2006) Three-dimensional reconstruction of a solid-oxide fuel-cell anode. Nat Mater 5(7):541–544. https://doi.org/10.1038/nmat1668

14. Xiang Y, Da YL, Zhong Z, Shikazono N, Jiao ZJ (2020b) Thermo-mechanical stress analyses of solid oxide fuel cell anode based on three-dimensional microstructure reconstruction. Int J Hydrog Energy 45(38):19791–19800. https://doi.org/10.1016/j.ijhydene.2020.05.121

15. Silling SA (2000) Reformulation of elasticity theory for discontinuities and long-range forces. J Mech Phys Solids 48(1):175–209. https://doi.org/10.1016/S0022-5096(99)00029-0

16. Silling SA, Askari E (2005) A meshfree method based on the peridynamic model of solid mechanics. Comput Struct 83(17–18):1526–1535. https://doi.org/10.1016/j.compstruc.2004.11.026

17. Silling SA, Bobaru F (2005) Peridynamic modeling of membranes and fibers. Int J Non-Linear Mech 40(2–3):395–409. https://doi.org/10.1016/j.ijnonlinmec.2004.08.004

18. Silling SA, Lehoucq RB (2008) Convergence of peridynamics to classical elasticity theory. J Elast 93(1):13–37. https://doi.org/10.1007/s10659-008-9163-3

19. Silling SA, Epton M, Weckner O, Xu J, Askari E (2007) Peridynamic states and constitutive modeling, vol 88. https://doi.org/10.1007/s10659-007-9125-1

20. Warren TL, Silling SA, Askari A, Weckner O, Epton MA, Xu JF (2009) A non-ordinary state-based peridynamic method to model solid material deformation and fracture. Int J Solids Struct 46(5):1186–1195. https://doi.org/10.1016/j.ijsolstr.2008.10.029

21. Ha YD, Bobaru F (2011) Characteristics of dynamic brittle fracture captured with peridynamics. Eng Fract Mech 78(7):1156–1168. https://doi.org/10.1016/j.engfracmech.2010.11.020

22. Agwai A, Guven I, Madenci E (2011) Predicting crack propagation with peridynamics: A comparative study. Int J Fract 171(1):65–78. https://doi.org/10.1007/s10704-011-9628-4

23. Wang HL, Oterkus E, Celik S, Toros S (2017) Thermomechanical analysis of porous solid oxide fuel cell by using peridynamics. AIMS Energy 5(4):585–600. https://doi.org/10.3934/energy.2017.4.585

24. Madenci E, Oterkus E (2014) Peridynamic theory and its applications, vol. 9781461484. https://doi.org/10.1007/978-1-4614-8465-3

25. Nayak S, Ravinder R, M KAN, Das S (2020) A peridynamics-based micromechanical modeling approach for random heterogeneous structural materials. Materials 13(6)

26. Kilic B, Madenci E (2010) An adaptive dynamic relaxation method for quasi-static simulations using the peridynamic theory. Theoret Appl Fract Mech 53(3):194–204. https://doi.org/10.1016/j.tafmec.2010.08.001

27. Luo Y, Ren L, Xie LZ, Ai T, He B (2017) Fracture Behavior Investigation of a Typical Sandstone Under Mixed-Mode I/II Loading Using the Notched Deep Beam Bending Method. Rock Mech Rock Eng 50(8):1987–2005. https://doi.org/10.1007/s00603-017-1227-x

28. Xiang Y, Da YL, Shikazono N, Jiao ZJ (2020a) Quantitative study on solid oxide fuel cell anode microstructure stability based on 3D microstructure reconstructions. J Power Sources 477:228653. https://doi.org/10.1016/j.jpowsour.2020.228653

29. Jordan L, Swanger WH (1930) The properties of pure nickel. Bur Stand J Res 5

30. Jiao ZJ, Shikazono N (2018) Prediction of Nickel Morphological Evolution in Composite Solid Oxide Fuel Cell Anode Using Modified Phase Field Model. J Electrochem Soc 165(2):55–63. https://doi.org/10.1149/2.0681802jes